Heat-release dynamics in a doubly-transcritical LO$_2$/LCH$_4$ cryogenic coaxial jet flame subjected to fuel inflow acoustic modulation

C. Laurent [a,*], G. Staffelbach [a], F. Nicoud [b], T. Poinsot [c]

[a] *CERFACS, 42 Avenue Gaspard Coriolis, Toulouse Cedex 1 31057, France*
[b] *IMAG, Univ. Montpellier, CNRS, Montpellier, France*
[c] *IMFT, Allée du Professeur Camille Soula, Toulouse 31400, France*

Abstract

Large Eddy Simulations are used to study the heat-release response to fuel inflow acoustic harmonic oscillations, in a coaxial jet flame where both reactants (O$_2$ and CH$_4$) are injected in a dense cryogenic state. The geometry is that of the academic test rig Mascotte, operated by ONERA (France), which high pressure operating conditions are relevant for the characterization of flame dynamics in Liquid Rocket Engines (LREs). The simulations, which are carried out with a real-gas fluid solver using a detailed kinetic scheme for CH$_4$ high-pressure oxycombustion, provide a thorough insight into the flame response for a wide range of forcing frequencies, spanning from approximately 1kHz to 20kHz. Local Flame Transfer Functions (FTF) are computed and analyzed: regions of preferential heat-release response are observed to be highly dependent on the forcing frequency. An analysis based on a flame sheet assumption is conducted to distinguish the main sources of heat release fluctuations: the primary contribution comes from the species diffusivity oscillations, while the density variations have a negligible effect. The second largest contributor is either the mixture fraction gradient or the flame surface area, depending on the forcing frequency. The FTFs are expected to be useful for thermoacoustic Low-Order Models or Helmholtz solvers, and the subsequent analysis has the potential to guide future development of analytical models for flame dynamics in LREs.
© 2020 The Combustion Institute. Published by Elsevier Inc. All rights reserved.

Keywords: Thermoacoustic instabilities; Cryogenic flame; Flame dynamics; Flame transfer function; Liquid rocket engine

1. Introduction

Since the early days of space exploration, thermoacoustic instabilities have been a major concern for Liquid Rocket Engine (LRE) designers, due to their ability to penalize entire industrial

* Corresponding author.
  E-mail address: laurent@cerfacs.fr (C. Laurent).

projects [1]. In order to reach greater reusability and maneuverability, the current launcher industry is now heading towards propulsion relying on high-pressure methane oxycombustion. In these systems, the propellants are injected through coaxial injectors under various thermodynamic conditions, including the so-called *doubly-transcritical* regime (LO_2/LCH_4) where both reactants are in a dense cryogenic state. The prediction of thermoacoustic instabilities, which result from a two-way coupling between acoustic waves and flames oscillations, is mandatory in the development of these novel combustion devices. However, little is known on the flame response to acoustic perturbations under these specific conditions, and a key challenge is therefore to gain a better understanding of physical phenomena governing heat-release dynamics in LRE cryogenic diffusion flames.

Earliest studies related to combustion in LRE conditions [2,3], which were mostly interested in canonical problems, found out that the mixing of cryogenic propellants at subcritical temperatures but supercritical pressures is controlled by turbulent mixing and a continuous pseudo-boiling transformation, also called *transcritical* transition. Later, Direct Numerical Simulations (DNS) and Large Eddy Simulations (LES) were employed to tackle more complex problems, including supercritical jet flames [4,5]. These numerical efforts were accompanied by experimental ones, most notably on the Mascotte test rig operated by ONERA (France) [6], where a doubly-transcritical LO_2/LCH_4 coaxial jet flame was first reported [7]. The interaction between supercritical flames and acoustic waves could be thoroughly investigated only very recently [8,9] in a variation of the Mascotte testbed comprising a few coaxial injectors. LO_2/GCH_4 flames were subjected to large amplitude transverse acoustic modes, that noticeably enhanced cryogenic O_2 pseudo-boiling and mixing, resulting in flattened, shorter dark cores, as well as more compact and intense heat-release regions. LES of comparable configurations led to identical observations [10,11], and were also used to explore LO_2/GH_2 flame dynamics during thermoacoustic limit-cycles in a 42-injectors rocket combustor [12,13]. It was proved that the flames located near velocity nodes have the largest contribution to the instability, and the gain and phase of the heat release response at the unstable frequencies were computed.

Anterior research efforts mostly studied the dynamics of supercritical LO_2/GCH_4 or GH_2 coaxial jet flames subjected to large amplitude transverse acoustic waves, for only a very few forcing frequencies. Strong acoustic perturbations have the merit of generating clearly visible dynamics, thus permitting macroscopic analyses of the dark core or the flame surface evolution, as in [9–12]. However, intense excitations may trigger nonlinear phenomena, and are not characteristic of the small

fluctuations that exist at the onset of an instability. As a result, previous works were mostly restricted to qualitative examinations: they did not compute a Flame Transfer Function (FTF) relating the fluctuations of heat-release to the acoustic forcing over a wide range of frequencies, nor did they provide sufficient quantitative information to guide the development of analytical flame response models. Thorough theroretical investigation of diffusion jet flames dynamics were conducted [14–16], but only for gaseous laminar systems which are too distant from LRE combustion.

To complete earlier research, the present work employs LES to characterize the dynamics of a doubly-transcritical LO_2/LCH_4 coaxial jet flame in the geometry of the single-injector Mascotte test rig [7], forced by fuel inflow acoustic modulation over a wide frequency range. To the knowledge of the authors, this is one of the first attempts to compute and analyze a complete FTF for a cryogenic coaxial jet flame, especially in the case of doubly-transcritical combustion, a thermodynamic regime arising in modern LREs but that is still little studied. The flame response is further analyzed through a comprehensive evaluation of the mechanisms contributing to heat-release fluctuations. Section 2 introduces the simulated configuration and the numerical methods employed. In Section 3, the unforced flame topology is briefly described. Finally, Section 4 presents the forced flame response, including the computed FTF and the analysis of heat-release dynamics contributions.

2. Operating conditions and numerical solver

The real-gas version of the LES solver AVBP [5,17] is employed to solve the three-dimensional reactive, multi-species, and compressible Navier-Stokes equations on unstructured meshes. Non-ideal thermodynamics are modeled thanks to the Soave-Redlich-Kwong (SRK) equation of state [18]:

$$p = \frac{\rho \bar{r} T}{1 - \rho b_m} - \frac{\rho^2 a_m(T)}{1 + \rho b_m} \qquad (1)$$

where $\bar{r}$ is the mixture gas constant, and b_m and $a_m(T)$ are defined as in [2]. Most numerical details of the simulations can be found in [5,19]. The TTG4A finite-element scheme [20] (3rd order in space, 4th in time) adapted for real-gas conditions is used. The σ-model [21] closes the subgrid stress tensor. Reaction kinetics are based on a detailed mechanism for high-pressure CH_4 oxycombustion [22,23], that was reduced from the GRI3.0 mechanism, and that contains 9 resolved species, 7 quasi-steady-state species, and 82 reactions. Molecular transport of species and energy are based on constant Schmidt and Prandtl numbers assumptions, combined with Chung's correlations [24].
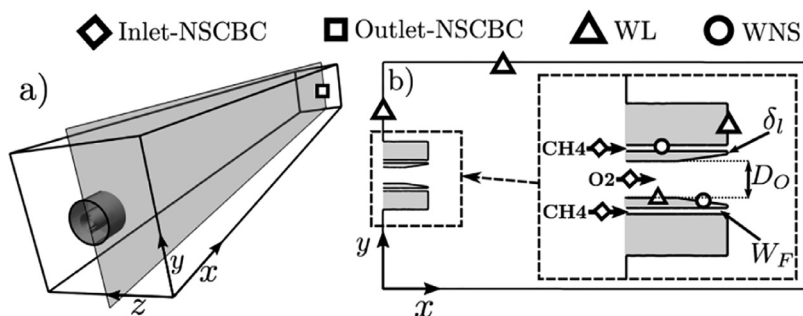
Fig. 1. (a) Three-dimensional view of the Mascotte test rig. (b) Closeup view of the near injector region. The symbols detail the boundary conditions in the simulation (WL: Law of the Wall, WNS: Resolved No Slip Wall).

Table 1

Injection conditions (mass flow rate, reduced pressures and temperatures). Momentum flux ratio $J = (\rho_{CH4}u_{CH4}^2)/(\rho_{O2}u_{O2}^2) = 33.3$, global equivalence ratio $\phi_g = 14.3$.

	$\dot{m}_{inj}/\dot{m}_{inj}^{O2}$	T_R^{inj}	P_R^{inj}
O_2	1.0	0.55	1.49
CH_4	3.59	0.62	1.64

Their subgrid scale counterparts rely on the gradient transport assumption, with turbulent Schmidt and Prandtl numbers fixed at 0.7.

The Mascotte geometry [7] (Fig. 1) is a parallelepipedic chamber with a coaxial injector at its backplate that comprises a central round injection of liquid oxygen (diameter D_O), surrounded by an annular injection of liquid methane (width W_F). Those are separated by a tapered lip of thickness δ_l at its tip. The boundary conditions for the simulation are shown in Fig. 1-(b). One-seventh power-law velocity profiles and synthetic turbulence [25] are imposed at both fuel and oxidizer inlets through NSCBC boundary conditions [26]. Acoustic wave modulation at the fuel inlet is performed with [27]. All wall boundaries are assumed adiabatic. This may be a strong assumption, as shown in [22], where the resolution of a conjugate heat transfer problem at the injector lip evidenced a complex and unsteady anchoring mechanism. However, in the absence of reliable wall temperature data, adiabatic conditions are still considered as state of the art in LES of LRE combustion. Thus, the evaluation of flame-wall interaction effects on the heat-release forced dynamics is left for future investigations.

Injection conditions summarized in Table 1 are identical to those in [22], and similar to the conditions T1 in [7] (except the pressure that is 75 bar instead of 54 bar). Computations are performed on a 3D unstructured mesh of 40 million tetrahedral cells, generated thanks to an adaptive mesh refinement algorithm based on physically relevant metrics, that is available in the open-source library MMG [28,29]. The mesh resolution in the near injector region is $\delta_l/30$ and is progressively coarsened downstream. The walls of both O_2 and CH_4 injection channels that are located near the injector exit are resolved, and no-slip conditions are applied. On the contrary, the upstream portion of the injection lines are not resolved and are rather modeled with a classical Law of the Wall. It is *a posteriori* verified that the wall coordinate y^+ is comprised between 2 and 7 at the lip tip, and between 5 and 10 in the reactants injection channels. In addition, a mesh sensitivity evaluation was conducted (Fig. S1 in Supplemental Material 1) and showed satisfactory agreement.

3. Flame topology and structure

In order to provide a better understanding of the flame response to acoustic perturbations, this section first briefly describes the unforced flame topology. This simulation was run and averaged over 25 ms, which is roughly 10 convective times necessary for a particle of fluid in the slow O_2 jet to reach the end of the flame. An instantaneous solution is presented in Fig. 2-(a), and averaged fields of density, axial velocity, and OH radical mass fraction are shown in Fig. 2-(b). The reader is also reported to Supplemental Material 1 (Fig. S1) for radial profiles of averaged quantities.

Remarkable features characteristic of confined cryogenic coaxial jet flames are observed. The dense O_2 core extends over a considerable length in the chamber, before being completely vaporized in a region of intense pseudo-boiling comprised between $x = 1.5D_O$ and $x = 4D_0$ from the injector exit (C_p contour in Fig. 2-(b)). Contrarily, the annular CH_4 jet experiences an earlier pseudo-boiling between $x = 0.5D_O$ and $x = 2D_O$, such that downstream of this location the fuel stream is in a light gaseous state. The dark core vaporization induces a significant dilatation of the oxidizer flow, that in turn provides radial momentum to the surrounding
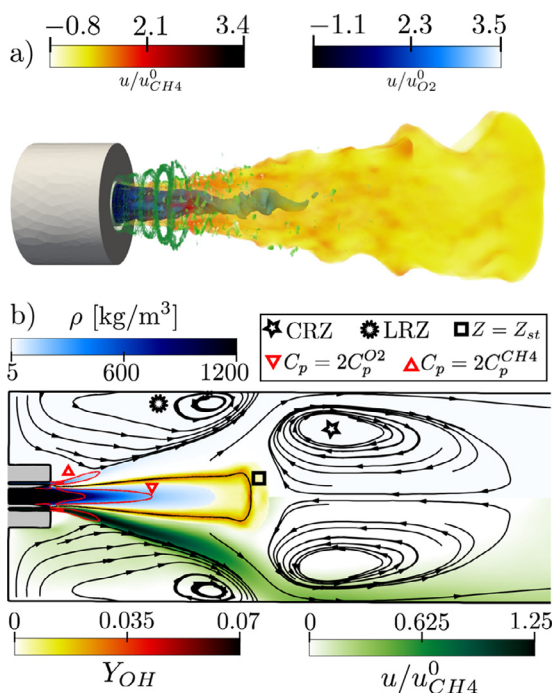
Fig. 2. (a) Yellow: instantaneous isosurface of temperature $T = 2000$K colored by axial velocity, blue: isosurface of density $\rho = 0.5\rho_{O2}^0$ colored by axial velocity, green: isosurface of Q-criterion $Q = (u_{CH4}^0/W_F)^2$. (b) Averaged fields of density (blue), axial velocity (green, only in the lower-half), and OH mass fraction (yellow). Red lines are contours of heat capacity C_p, the dark line marked by a square is the contour of stoichiometric mixture fraction $Z = Z_{st} = 0.2$. Lines with arrows are the flow streamlines. CRZ: Central Recirculation Zone, LRZ: Lateral Recirculation Zone. (For interpretation of the references to color in this figure legend, the reader is referred to the web version of this article.)

flame and light methane jet. As a result, this one mixes with hot combustion products, is pushed outwards, and the streamlines deviate from their original trajectory to impinge on the chamber wall. The impact of this fast and light fluid on the solid boundary generates two large recirculation zones: the Central Recirculation Zone (CRZ) and the Lateral Recirculation Zone (LRZ). Upstream of this divergence, the CH_4 annular jet has a constant opening angle of $17°$, while the flame (Mixture fraction contour in Fig. 2-(b)) is narrower with a nearly constant opening angle of $5°$. The flame lies in a region of low axial velocity, and its thin flame brush indicates that it is relatively stable with limited displacements. Its length is $L_f = 13.3D_O$, and it terminates abruptly in a region where it encounters the strong adverse flow of the CRZ. Note that the flame is anchored at the injector lip, and no triple-flame is observed, which is a direct consequence of the use of adiabatic boundary conditions.

Fig. 2-(a) reveals rich dynamics in the physical processes described above. Jet breakup causes detachment of pockets of cryogenic O_2 from the dark core, which results in intermittent vaporization and mixing. Isosurfaces of Q-criterion evidence vortex rings that are formed at the methane injector exit and convected downstream in the annular jet

with a clearly identifiable wavelength, which suggests that they may result from a Kelvin-Helmholtz instability. These coherent wave-like patterns also visibly affect the flame surface. Although these unsteady phenomena may participate in the flame response to imposed acoustic perturbations, the thorough study of the interaction between intrinsic and forced dynamics is out of the scope of this paper and is left for future work.

4. Heat-release dynamics forced by acoustic modulation

Distinct simulations are performed to impose acoustic harmonic perturbations at the fuel inlet, for 16 forcing frequencies f comprised in the range $\mathcal{O}(1\text{kHz}) - \mathcal{O}(20\text{kHz})$. The targeted modulation inlet velocity reads:

$$u'_{CH4} = Au_{CH4}^0 \sin(2\pi f t) \qquad (2)$$

This pulsation is imposed through the method proposed in [27]: the actual fluctuating inflow velocity may then slightly differ from Eq. (2) in order to avoid the reflection of acoustic waves at the fuel inlet. Since the goal is to evaluate the flame *linear* response to these modulations, the excitation
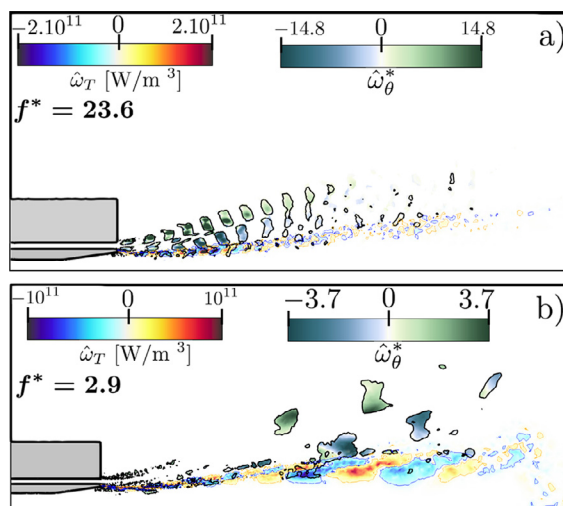
Fig. 3. (a) Maps of the Fourier coefficients for a high-frequency forcing ($f^* = 23.6$). Dark lines: contour of $\hat{Q}$-criterion, colored by the normalized azimuthal vorticity $\hat{\omega}_\theta^* = (\hat{\omega}_\theta W_F)/(A u_{CH4}^0)$. Blue-red: Fourier coefficient of the heat-release rate $\hat{\omega}_T$. (b) Same, for a low-frequency forcing ($f^* = 2.9$). (For interpretation of the references to color in this figure legend, the reader is referred to the web version of this article.)

amplitude $A u_{CH4}^0$ is low ($A = 0.025$), such that it is characteristic of the onset of an instability. This linearity is *a posteriori* verified by performing additional computations at different forcing amplitudes; comparisons are provided in Supplemental Material 3. Each simulation is run for at least 20 periods to ensure the dissipation of transients and the convergence of Fourier statistics. Modulations at the oxidizer inlet were also attempted, but no noticeable flame response was observed. Since the bulk flow velocity u_{O2}^0 is roughly one order of magnitude lower than u_{CH4}^0, such forcing produces very small absolute value perturbations, which are difficult to detect using Fourier analysis due to the ambient turbulent noise. As a result, it is not guaranteed that this apparent absence of flame response to acoustic excitation at the oxidizer inflow is stemming from a physical phenomenon, or simply the consequence of signals that are too weak to be clearly identified.

Due to the high-frequency of LRE thermoacoustic instabilities and the length of coaxial jet flames, the heat-release region is not assumed acoustically compact (a usual hypothesis for gas-turbine combustion): therefore all quantities depend on both the forcing frequency f and the axial location x. In the following, the normalized quantities $f^* = f L_f/u_{CH4}^0$ and $x^* = x/L_f$ are used, and for any variable v, the Fourier coefficient at the forcing frequency f^* is noted $\hat{v}$.

4.1. Flame transfer function

The imposed acoustics perturbations produce remarkably different responses, depending on the forcing frequency f^*. This is evidenced in Fig. 3, where the Fourier transforms of azimuthal vorticity and heat-release are mapped for a low-frequency forcing ($f^* = 2.9$ in Fig. 3-(b)), and a high-frequency one ($f^* = 23.6$ in Fig. 3-(a)). When they exit the fuel injector, acoustic waves generate shear, which in turn produces pairs of counter-rotating vortex rings that are convected downstream in the annular jet. At high-frequency these vortices are generated directly at the injector nozzle and are convected over a length of roughly $0.4 L_f$ before dissipating. Conversely, at low-frequency the larger vortex rings are engendered more downstream (at approximately $x = 0.5 L_f$) and are transported to the end of the flame. When vortices travel in the vicinity of the flame, they generate a variable strain rate that induces flame fluctuations: there exist therefore a strong correlation between these dinstictive vortex dynamics and the resulting heat-release oscillations. At $f^* = 23.6$, the heat-release response concentrates in a thin layer extending from the injector exit to $x = 0.3 L_f$ in the wake of the lip. In contrast, for $f^* = 2.9$, $\hat{\omega}_T$ has a lower intensity, but is distributed over a longer and wider area mostly lying in the second half of the flame. The broader heat-release brush suggests in this case important flame displacements.

To provide a quantitative evaluation of the flame forced dynamics, a FTF relating the heat-release fluctuations to the acoustic excitation is defined in the frequency domain:

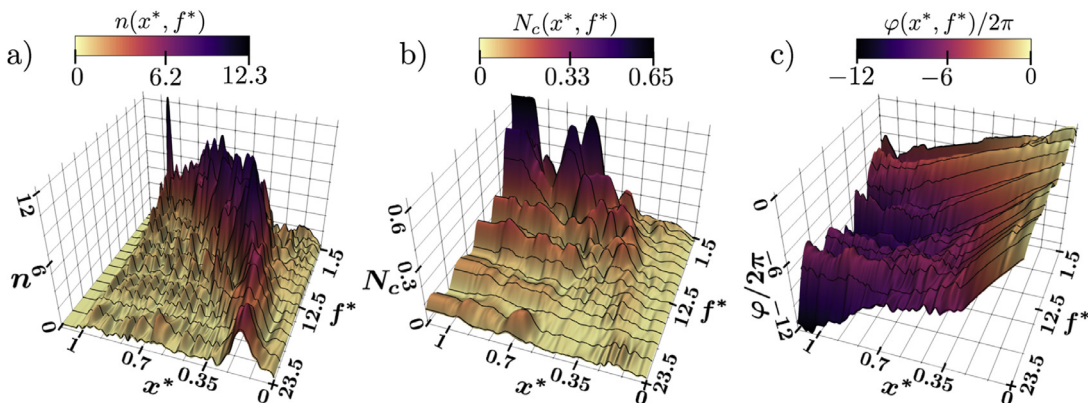$$\frac{(\hat{Q}/Q_0)}{(\hat{u}/u_0)} = \frac{L_f}{Q_0(\hat{u}/u_0)} \int_0^1 \hat{q}(x^*)dx^* \tag{3}$$

Fig. 4. (a) Local FTF gain $n(x^*, f^*)$. (b) Cumulative FTF gain $N_c(x^*, f^*)$. (c) Local FTF phase $\varphi(x^*, f^*)$. The dark lines are points directly computed from the 16 forced frequencies. For vizualisation purposes the surfaces were obtained by cubic spline interpolation along the f^* axis.

where Q_0 and $\hat{Q}$ are the averaged and fluctuating global flame power, u_0 and $\hat{u}$ are the averaged and fluctuating bulk velocity in the fuel injector near its outlet, and $\hat{q}(x^*)$ is the fluctuating heat-release per unit length. The local FTF gain $n(x^*, f^*)$ and phase $\varphi(x^*, f^*)$ are defined as:

$$\frac{L_f \hat{q}(x^*)}{Q_0(\hat{u}/u_0)} = n(x^*, f^*)e^{j\varphi(x^*, f^*)} \qquad (4)$$

A cumulative FTF gain $N_c(x^*, f^*)$ is also defined:

$$N_c(x^*, f^*) = \left| \frac{L_f}{Q_0(\hat{u}/u_0)} \int_0^{x^*} \hat{q}(x^*)dx'^* \right| \qquad (5)$$

Note that $N_c(x^* = 1, f^*)$ corresponds to the global gain of the entire flame, and that if the flame were compact then the local gain $n(x^*, f^*)$ would be uniformly equal to the global gain. The local FTF is displayed in Fig. 4. Computed data points are available in Supplemental Material 2.

The local FTF gain map (Fig. 4-(a)) corroborates observations already made above: at low-frequency forcing the region of strongest heat-release response is long and spans over the entire second half of the flame. As the excitation frequency increases, this region shortens and shifts upstream, such that for high-frequency forcing it is localized at the injector exit. This evolution of the preferential response region is a direct consequence of the vortex rings dynamics described earlier. The local FTF phase (Fig. 4-(c)) behaves similarly: for low f^* it is a linear function of x^* over the entire flame, which indicates a constant disturbance propagation speed u_{prop} along the axial direction. For higher f^*, the portion of constant propagation speed shrinks: it only extends from $x^* = 0$ to $x^* = 0.3$ at $f^* = 23.6$. Downstream of this location, the local phase reaches a plateau where it stagnates (i.e. the heat-release presents in-phase bulk oscillations). The shape of this plateau corresponds

to the upper boundary of the strongest response region in Fig. 4-(a). In addition, u_{prop} increases with frequency: for $f^* = 1.5$, $u_{prop} = 0.35u_{CH4}^0$, while $u_{prop} = 1.1u_{CH4}^0$ for $f^* = 23.5$. In its linear portion, the phase evolves rapidly with x^*, which results in heat-release fluctuations that are spatially out of phase. Conversely, points within the plateau oscillate in-phase. This directly affects the cumulative gain (Fig. 4-(b)), that shows that the second half of the flame has always the largest contribution to the overall heat-release response. Indeed, even though responses are relatively small in the plateau, they oscillate synchronously, and therefore produce a strong overall contribution. On the contrary, heat-release fluctuations in the preferential response region are not synchronized due to a fast propagation, and thus cancel each other out. Finally, note that the local gain largely exceeds those typical of gas-turbine flames, whereas the global gain has more usual values.

4.2. Analysis of heat-release dynamics contributions

The distinct physical contributions to the forced heat-release dynamics are here evaluated through a comprehensive analysis. The reaction layer is assumed to be the infinitely thin sheet corresponding to the isosurface $Z = Z_{st}$. Following [14], the local heat-release per unit length writes:

$$q(x^*, t) = \left[\rho \mathcal{D} \left| \frac{\partial Z}{\partial n} \right| \left(\left| \frac{\partial Y_O}{\partial Z} \right| + \left| \frac{\partial Y_F}{\partial Z} \right| \right) \xi h_R \right]_{Z=Z_{st}} \qquad (6)$$

where $\mathcal{D}$ is the species diffusivity coefficient, $\partial Z/\partial n$ is the mixture fraction gradient in the direction normal to the flame sheet, Y_O and Y_F are the oxidizer and fuel mass fractions, ξ is the local mean flame radius (i.e. the flame surface density per unit length),
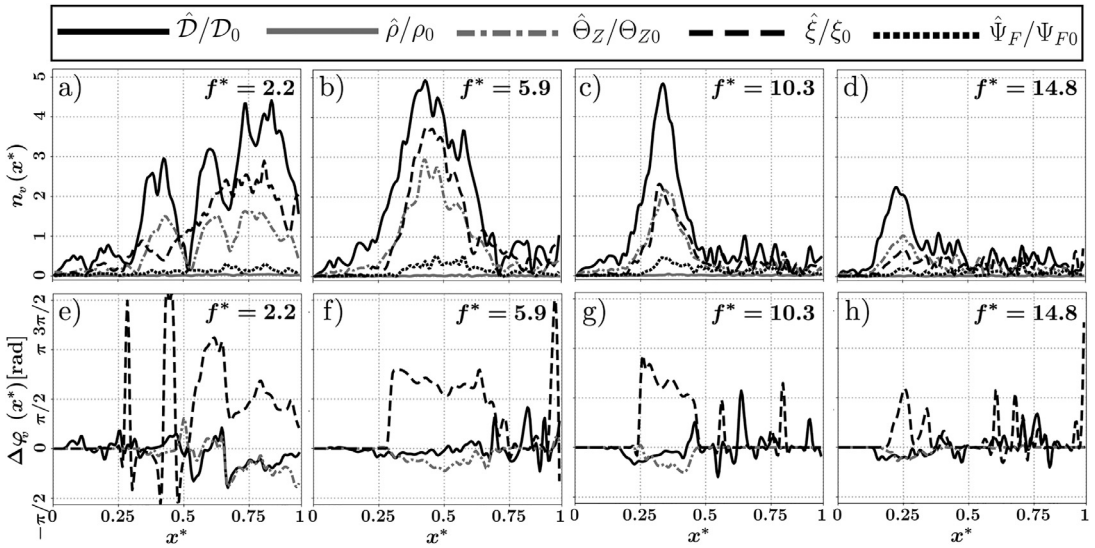
Fig. 5. (a)-(d) CTF gains n_v along the flame axis, at 4 forcing frequencies. (e)-(h) Same, for the CTF phase shift $\Delta\varphi_v$ along the flame axis. Phase-shift values between $-\pi/2$ and $\pi/2$ indicate positive contributions the the heat-release response, while values between $\pi/2$ and $3\pi/2$ are negative contributions.

and h_R is the heat of reaction per unit mass of reactants burnt (assumed constant). After splitting each variable v into its mean (v_0) and fluctuating (v') parts, a linearization of Eq. (6) followed by a Fourier transform yields:

$$\frac{\hat{q}}{q_0} = \left[\frac{\hat{\rho}}{\rho_0} + \frac{\hat{\mathcal{D}}}{\mathcal{D}_0} + \frac{\hat{\Theta}_Z}{\Theta_{Z0}} + \frac{\hat{\Psi}_F}{\Psi_{F0}} + \frac{\hat{\xi}}{\xi_0} \right]_{Z=Z_{st}} \quad (7)$$

where $\Theta_Z = |\partial Z / \partial n|$ is related to the mixing rate in the physical space, and $\Psi_F = |\partial Y_O / \partial Z| + |\partial Y_F / \partial Z|$ is linked to the internal flame structure in the mixture fraction space.

In Eq. (7), the local-heat release fluctuations are decomposed into 5 distinct contributions v. Similarly to Eq. (4), a Contribution Transfer Function (CTF) is defined for each one of those:

$$\frac{L_f q_0 \hat{v}(x^*)}{Q_0 v_0 (\hat{u}/u_0)} = n_v(x^*, f^*) e^{j\varphi_v(x^*, f^*)} \quad \Delta\varphi_v = \varphi_v - \varphi \quad (8)$$

where $\Delta\varphi_v(x^*, f^*)$ is the phase shift of the fluctuations of v, with respect to those of the local heat-release per unit-length $q(x^*)$. The species diffusivity $\mathcal{D}$ is computed as the mass fraction average of those of CH_4 and O_2, and includes both molecular and turbulent diffusion. Unsteady flame sheets are extracted from the simulations, and the individual CTFs are displayed in Fig. 5.

The CTF gains (Fig. 5(a)–(d)) behave similarly as those in the FTF of Sec. 4.1: for high-frequency forcing, all contributions are the highest near the injector, while at lower frequencies they prevail in a wider region located more downstream. Density

fluctuations are remarkably low, which could seem surprising in a flow where dense cryogenic fluids co-exist with light burnt gases. It is however consistent with [30], where the structure of transcritical counterflow diffusion flames was shown to consist of a vaporization zone without any reaction occurring, followed by a gaseous reactive layer. Consequently, density fluctuations in the perturbed cryogenic methane jet vanish before reaching the flame surface, under the effect of the intense pseudo-boiling. Internal flame structure variations (represented by the term $\hat{\Psi}_F$) participate to the heat-release response in a larger extent than density, but are still roughly one order of magnitude lower than the others. The vortices-induced strain rate is significantly smaller than its extinction limit, and is therefore not sufficient to disturb the flame structure from its *flamelet* regime. Diffusivity fluctuations are the overall major contributor: the heat-release response is mostly driven by the faster or slower diffusion of reactants towards the flame front, which affects the local fluxes and results in variations of the mass burning rate. These diffusivity fluctuations may originate from both turbulent mixing variations, caused by the vortices strain-rate, and molecular diffusion oscillations engendered by pressure waves that accompanied these vortex-rings. The secondary contributor is frequency dependent: at high f^* it is the mixture fraction gradient fluctuations $\hat{\Theta}_Z$ in the near injector region, in agreement with previous studies in laminar gaseous diffusion jet flames [14–16]. At $f^* = 10.3$ (Fig. 5-(c)) a balance is reached between $\hat{\Theta}_Z$ and the flame surface area contribution $\hat{\xi}$. At low f^* the trend in-

verts and $\hat{\xi}$ prevails in the second half of the flame. The relative participations of $\hat{\Theta}_Z$ and $\hat{\xi}$ can be explained by the flame topology (Fig. 2-(b)). Near the injector the flame is strongly stabilized by an important shear and is confined between the two dense cryogenic jets: it is not easily displaced by the vortex-induced strain-rate, which rather affects the mixing efficiency through the mixture fraction gradient (see the thin heat-release response layer in Fig. 3-(a)). Conversely, when vortices are generated downstream at lower frequencies, they strain a portion of the flame lying in a light gaseous flow with lower shear, where the flame is only weakly stabilized and can therefore be easily displaced (see the broader heat-release response layer in Fig. 3-(b)). Finally, the examination of CTF phase shifts in Fig. 5(e)-(h) shows that both diffusivity and mixture fraction gradient oscillate nearly in phase with the local-heat release, and have therefore a positive contribution. On the contrary, flame surface area mostly fluctuates in phase quadrature ($\Delta\varphi_\xi = \pi/2$) or phase opposition ($\Delta\varphi_\xi = \pi$) with $q'(x)$, and has hence an adverse effect that tends to limit the local response strength. The vortex-rings dynamics are once again responsible for this behavior: as a vortex travels in the vicinity of the flame it enhances the local burning rate ($q'(x) > 0$) through higher-strain rate ($\Theta'_Z > 0$) and faster diffusion ($\mathcal{D}' > 0$), but simultaneously contracts the flame inwards ($\xi' < 0$).

5. Conclusions

Several LES have been performed to explore the forced dynamics of a doubly-transcritical LO$_2$/LCH$_4$ LRE jet flame, subjected to small amplitude acoustic forcing at the fuel injector. These computations were a numerical challenge that required 18.5 million CPU hours on a machine equipped with Intel Xeon 8168 processors (2.7 GHz). The heat-release response appeared to be directly controlled by the dynamics of vortex-rings pairs traveling in the fuel annular jet. The computation of a non-compact FTF over the range $\mathcal{O}(1\text{kHz}) - \mathcal{O}(20\text{kHz})$ revealed frequency-dependent preferential flame response regions, strongly correlated to the area of vortex generation and convection: the higher the excitation frequency, the closer to the injector both regions are localized. Additionally, the FTF data is available, and expected to be embedded in acoustic solvers for the prediction of thermoacoustic instabilities in multi-injectors LREs. In addition, a comprehensive analysis of the heat-release dynamics evidenced 3 major contributions to the flame response: the variations of species diffusivity that globally dominate, those of mixture fraction gradient that are significant at high-frequency, and the flame surface area fluctuations that become stronger at low-frequency. This analysis has the potential to guide future development of theoretical models for LRE flame

response, which are expected to account for the 3 major contributions identified.

Note that LES was here employed as a purely exploratory tool to investigate physical mechanisms difficultly reproducible experimentally. Thus, results presented in this work were not validated against experimental data. This advocates the need to design novel advanced test rigs to enable the thorough study of cryogenic flame dynamics in extreme conditions characteristic of LREs.

Declaration of Competing Interest

The authors declare that they do not have any financial or nonfinancial conflict of interests

Supplementary material

Supplementary material associated with this article can be found, in the online version, at doi: 10.1016/j.proci.2020.05.051.

References

[1] J.C. Oefelein, V. Yang, *J. Propul. Power* 9 (5) (1993) 657–677.
[2] V. Yang, *Proc. Combust. Inst.* 28 (1) (2000) 925–942.
[3] J. Bellan, *Prog. Energy Combust. Sci.* 26 (4) (2000) 329–366.
[4] J.C. Oefelein, *Proc. Combust. Inst.* 30 (2) (2005) 2929–2937.
[5] T. Schmitt, Y. Méry, M. Boileau, S. Candel, *Proc. Combust. Inst.* 33 (1) (2011) 1383–1390.
[6] L. Vingert, M. Habiballah, P. Vuillermoz, S. Zurbach, *51st International Astronautical Congress, Rio de Janeiro, Brazil, 2000* (2000).
[7] G. Singla, P. Scouflaire, C. Rolon, S. Candel, *Proc. Combust. Inst.* 30 II (2) (2005) 2921–2928.
[8] F. Richecoeur, P. Scouflaire, S. Ducruix, S. Candel, *J. Propuls. Power* 22 (4) (2006) 790–799.
[9] Y. Méry, L. Hakim, P. Scouflaire, L. Vingert, S. Ducruix, S. Candel, *Comptes Rendus - Mecanique* 341 (1–2) (2013) 100–109.
[10] L. Hakim, T. Schmitt, S. Ducruix, S. Candel, *Combust. Flame* (2015).
[11] L. Hakim, A. Ruiz, T. Schmitt, M. Boileau, G. Staffelbach, S. Ducruix, B. Cuenot, S. Candel, *Proc. Combust. Inst.* 35 (2) (2015) 1461–1468.
[12] A. Urbano, Q. Douasbin, L. Selle, G. Staffelbach, B. Cuenot, T. Schmitt, S. Ducruix, S. Candel, *Proc. Combust. Inst.* 36 (2) (2017) 2633–2639.

[13] S. Gröning, J.S. Hardi, D. Suslov, M. Oschwald, *J. Propuls. Power* (32) (2016) 560–573.

[14] N. Magina, D.H. Shin, V. Acharya, T. Lieuwen, *Proc. Combust. Inst.* 34 (1) (2013) 963–971.

[15] N.A. Magina, T.C. Lieuwen, *Combust. Flame* 167 (2016) 395–408.

[16] Y. Tang, J. Zhuo, W. Cui, S. Li, Q. Yao, *Combust. Flame* 204 (2019) 58–67.

[17] V. Moureau, G. Lartigue, Y. Sommerer, C. Angel-berger, O. Colin, T. Poinsot, *J. Comput. Phys.* 202 (2) (2005) 710–736.

[18] G. Soave, *Chem. Eng. Sci.* 27 (6) (1972) 1197–1203.

[19] T. Schmitt, L. Selle, A. Ruiz, B. Cuenot, *AIAA J.* 48 (9) (2010) 2133–2144.

[20] O. Colin, M. Rudgyard, *J. Comput. Phys.* 162 (2) (2000) 338–371.

[21] F. Nicoud, H.B. Toda, O. Cabrit, S. Bose, J. Lee, *Phys. Fluids* 23 (8) (2011) 085106.

[22] C. Laurent, L. Esclapez, D. Maestro, G. Staffel-bach, B. Cuenot, L. Selle, T. Schmitt, F. Duchaine, T. Poinsot, *Proc. Combust. Inst.* 37 (4) (2019) 5147–5154.

[23] C. Laurent, A reduced kinetic mechanism for CH4 LRE combustion, 2019, (http://chemistry.cerfacs.fr/en/chemical-database/mechanisms-list/ch4_10_82_7_cl-arc-mechanism).

[24] T.H. Chung, M. Ajlan, L.L. Lee, K.E. Starling, *Ind. Eng. Chem. Res.* 27 (4) (1988) 671–679.

[25] A. Smirnov, S. Shi, I. Celik, *ASME Fluids Engineering Division Summer Meeting*, 11215, 2000.

[26] T.J. Poinsot, S. Lele, *J. Comput. Phys.* 101 (1) (1992) 104–129.

[27] A. Kaufmann, F. Nicoud, T. Poinsot, *Combust. Flame* 131 (4) (2002) 371–385.

[28] C. Dobrzynski, P. Frey, in: Proceedings of the 17th international Meshing Roundtable, Springer, 2008, pp. 177–194.

[29] C. Dapogny, C. Dobrzynski, P. Frey, *J. Comput. Phys.* 262 (2014) 358–378.

[30] G. Lacaze, J.C. Oefelein, *Combust. Flame* 159 (6) (2012) 2087–2103.